Influence of pilot H2 injection on methane-air swirled flame stabilization and acoustic response

Andrea Aniello, Davide Laera, Sylvain Marragou, Thierry Poinsot, T. Schuller, Laurent Selle

Version of Record: https://www.sciencedirect.com/science/article/pii/S0010218023001335
Manuscript_dd2e5ad486815ae19b7346e0ecc17063

Influence of pilot H_2 injection on methane-air swirled flame stabilization and acoustic response

A. Aniello[a,*], D. Laera[b,c], S. Marragou[a], T. Poinsot[a], T. Schuller[a], L. Selle[a]

[a] *Institut de Mécanique des Fluides de Toulouse, IMFT, Université de Toulouse, CNRS, 31400 Toulouse, France*
[b] *CERFACS, 42 avenue Gaspard Coriolis, 31057 Toulouse, France*
[c] *Department of Mechanics, Mathematics and Management - Polythechnic of Bari, Via Re David, 200, 70125 Bari, Italy*

Abstract

Large Eddy Simulation is used to investigate the effect of localized pilot H_2 injection on the Flame Transfer Function (FTF) of a premixed CH_4-air swirled flame. The response of a perfectly premixed methane-air flame is compared to the one with an additional pilot hydrogen injection that supplies 10% of the original power. Numerical simulations are validated against experiments in terms of global FTF values at selected forcing frequencies, acoustic pressure and velocity signals, CH^* flame images and flame root position dynamics. The unforced cases are first considered showing that, when H_2 is injected in the center, the flame becomes slightly lifted with a localized diffusion front above the pilot injection. As in the experiments, LES retrieves that hydrogen pilot injection leads to a global redistribution of the heat release rate towards the flame root due to higher burning rates which translates to an overall FTF gain reduction over the entire frequency range

*Corresponding author: andrea.aniello.92@gmail.com

explored. Then, the flame acoustic response for the two injection strategies is scrutinized at two distinct forcing frequencies: 240 Hz where the FTF gain difference is maximum, and 590 Hz where the FTF phase shift is maximum. LES reveals that, despite H_2 pilot injection does not modify the dynamics of the large vortical structures shed in the external shear layer of the swiling jet which are synchronized by the acoustic forcing, the redistribution of the heat release rate towards the flame base weakens their interaction with the flame tip, explaining partly the FTF gain reduction at the two selected frequencies. In addition to that, a marked axial movement of the internal recirculation zone is observed at 240 Hz during the forcing cycle. For the pilot injection, it leads to an oscillation of the lifted flame root while, for the CH_4-air case, the flame anchoring point is not affected. This additional oscillation leads for the pilot case to heat release rate fluctuations acting in phase opposition with respect to those observed at the flame tip, generating a further drop of the FTF gain at this specific frequency. The increased burning rate at the flame root and the flame length reduction of the pilot hydrogen flame also affect the characteristic time lag of the flame response. For both frequencies $f = 240$ Hz and 590 Hz, the phase shift between the two injection strategies is proportional to the flame length reduction caused by hydrogen injection. These simulations confirm that pilot hydrogen injection is an efficient way to reduce the acoustic response of swirled flames over a large frequency bandwidth.

Keywords: Hydrogen enrichment, Swirled flow, Flame stabilization, Flame

1. Introduction

Recent years have seen the necessity to reduce the carbon foot-print of power and transport sectors in order to fulfill stricter emission regulations and mitigate global warming. This objective has driven the recent push for the use of hydrogen as decarbonized fuel for land-based gas turbines and aerojet engines [1, 2], opening new challenges in the context of thermoacoustic instabilities [3–5].

The transport and chemical properties of H_2 [6], differing from the ones of standard hydrocarbons, substantially modifies fundamental combustion characteristics leading to different flame responses to acoustic perturbations. For instance, the higher consumption speed [7–9] and the greater strain resistance [10, 11] of H_2-enriched blends reduce the flame length [12] and could also promote the transition from V- to M-shape stabilization [13–16]. These changes directly affect the stability of the combustor [17–20] because thermoacoustic instabilities originate from a constructive coupling between acoustic oscillations and heat release rate fluctuations, hence they are highly dependent on the flame shape.

A comprehensive review on the effect of hydrogen addition on flame dynamics was recently proposed by Beita *et al.* [21]. In this respect, the impact of H_2 addition on the FTF of jet premixed methane-air flames stabilized on a central bluff body was highlighted in [19, 22]. It was shown that, at constant total thermal power, hydrogen addition decreases (respectively increases) FTF gain at low (respectively high) frequencies and increases the

cut-off frequency. These studies also showed that, thanks to the high burning rate of hydrogen, the FTF phase reduces almost linearly with the H_2 concentration in the fuel blend. Similar results have also been found in recent simulations [23, 24].

Hydrogen enrichment also modifies the flame acoustic response of hydrocarbon swirl-stabilized flames [25, 26]. In such a configuration, however, the effects of hydrogen addition combine with other mechanisms controlling the FTF of a swirled flame, like for example in [27], making the interpretation of results less straightforward. In this regard, the acoustic response of a premixed methane-air flame with H_2-enrichment up to 40%vol was investigated in a dual-nozzle swirl stabilized combustor [28]. The hydrogen addition modified the response of the flame tip to the acoustic perturbations, resulting in a gain reduction and in a global phase shift of the FTF. A modification of the flame-vortex interaction due to hydrogen addition was also highlighted in [29], where either transient or steady variations of H_2 content in natural gas-air mixture were used to control thermoacoustic instabilities in a technically premixed injection system. This study showed that the onsets of instability were highly repeatable irrespective of the duration of H_2 injection, while the transitions from unstable to stable operation were not always consistent. This variance was justified with the increasing temperature of the centerbody favored by hydrogen injection, which was ultimately affecting the flame response. A further investigation about the effect of H_2 enrichment on the thermoacoustic behavior of a burner was recently conducted

in an annular combustion chamber [30], demonstrating that H_2 has a non-linear influence on the development of azimuthal self-sustained instabilities. Thermo-acoustic instabilities were maximized for a certain hydrogen content and decreased for further H_2 additions. In the same study it was also shown that pressure variation could produce a stabilizing or destabilizing effect depending on the hydrogen content.

In all aforementioned cases, when blended with another fuel, hydrogen is always injected fully premixed. Nevertheless, the adoption of radially-stratified mixtures was also proposed to improve the combustion stability of swirling flames, like for instance in [31–33]. To this regard, the use of a pilot injection has been also proposed as a technical solution to stabilize swirling natural-gas flames [34, 35]. In the same way, recent experimental results on a swirled coaxial injector have shown that a small central H_2 injection can modify the stability maps of a system operated with premixed methane-air mixtures [36]. Interestingly, this outcome was not found neither by premixing H_2 with the CH_4-air mixture in the main annular channel, nor via the pilot injection of pure-CH_4 in the central tube, but the fundamental mechanisms driving the change of flame dynamics were not clarified. Flame Describing Functions (FDF) of this configuration were also measured experimentally [37] showing that the change of the non-linear flame acoustic response in case of pilot H_2 injection was mainly due to the redistribution of heat release rate towards the flame root. However, the influence of this pilot injection on the velocity field and on the flame stabilization was not in-

vestigated. This specific configuration was also studied via Large Eddy Simulations [38], showing the importance of accounting for complex transport properties to predict the correct flame characteristics with H_2 addition for a steady flow. Nevertheless, this previous study considered only a low hydrogen content limited to 2% by power. The present work, instead, increases the H_2 substitution up to 10% by power and aims at elucidating the fundamental mechanisms that control the flame response to acoustic perturbations when the pilot-H_2 injection is added to a perfectly premixed methane-air flame. The second objective is to analyze the impact of the central pilot injection on the velocity field and on the flame root stabilization dynamics, which was neglected in the previous experimental investigation of the unsteady flame response [37].

The numerical setup is described in Sec. 2. Validation and analysis of the two injection strategies for the unforced cases are provided in Sec. 3 by comparing simulations with experimental results. Forced flow conditions for perfectly premixed methane-air mixture and with the addition of pilot hydrogen injection are validated and analyzed in Sec. 4, where the impact of the pilot H_2 is presented and its implication on the flame response discussed.

2. Experimental conditions and numerical setup

The experimental bench corresponds to the MIRADAS setup from IMFT laboratory [36]. The bottom of the combustor is made of a cylindrical plenum, followed by a convergent section that produces a top-hat laminar

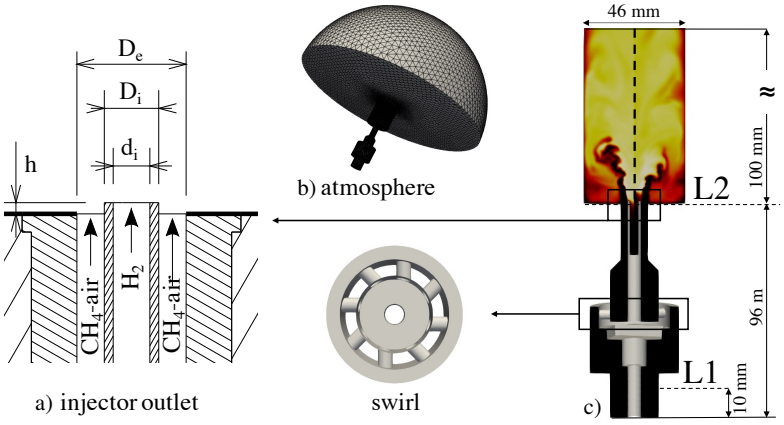

Fig. 1: Description of the numerical setup with the close up of the injector outlet (a), the dome representing the atmosphere (b) and the dgeometry of the injector (c) with the definition of the locations $L1$ and $L2$.

velocity profile. This flow feeds the external duct of a coaxial injector with external diameter D_e= 12 mm and internal diameter D_i=6 mm, as shown in Fig. 1. This annular duct is equipped with a radial swirler made of 8 radial tangential inlets to produce a rotating flow. The central injection tube has an internal diameter d_i= 4 mm and protrudes inside the combustion chamber by $h = 1.25$ mm. The flame is confined in a quartz tube featuring a diameter of 46 mm and a length of 100 mm that yields a full optical access.

Two operating conditions characterized by alternative injection strategies are investigated. In the first case, named REF, a fully premixed CH_4-air mixture is injected only in the annular swirling duct of the combustor as shown in Fig. 1(a). In the second case, named $PH10$, the methane flow rate in the annular channel is reduced and a complementary H_2 flow rate is added via the central pilot line in order to supply 10% of the total thermal power

P_{th} = 4 kW. This amount of hydrogen corresponds roughly to 25%vol in the fuel, which is aligned with the maximum H_2 content allowed in already existing combustion systems according to the current legislation. In this second case the air mass flow rate is kept constant, the variation of the bulk velocity U_b in the annular duct is negligible and the global equivalence ratio ϕ varies by less than 2%. The operating conditions of REF and $PH10$ cases are summarized in Table 1. When the system is submitted to the acoustic forcing, only the annular channel that supplies the CH_4-air mixture is subjected to the flow modulation. The hydrogen stream remains undisturbed throughtout the study. Measurements of acoustic velocity u' and pressure p' are taken upstream the swirler, at location $L1$ in Fig. 1(c). Moreover, the acoustic velocity is also reconstructed at the injector outlet (location $L2$) with the low order model described in [36].

LES is performed with the AVBP solver (www.cerfacs.fr/avbp7x/) and the computational domain includes the swirled coaxial injector and the cylindrical combustion chamber, as displayed in Fig. 1(c). Part of the surrounding around the chamber outlet is also simulated avoiding the specification of any numerical impedance at the combustion chamber outlet (Fig. 1(b)). The dynamic version of the thickened flame model (DTFLES) [39] is only triggered

Case	Annular		Pilot	Global
	$\dot{m}_{Air}$ (g/s)	$\dot{m}_{CH_4}$ (mg/s)	$\dot{m}_{H_2}$ (mg/s)	ϕ
REF	1.69	79.1	-	0.800
$PH10$	1.69	71.2	3.30	0.787

Table 1: Mass flow rates of air, methane and hydrogen with respective global equivalence ratios adopted for the two operating conditions.

in case of premixed combustion, while the diffusion flame front resulting from H_2 laminar pilot injection is fully resolved prescribing a proper grid resolution as in [38]. Wall heat losses are accounted for by specifying proper thermal resistances and imposing the experimental temperature profiles measured along the combustion chamber walls T_c, at the burner lips T_l and over the combustor backplane T_b. The temperature of the external side of the combustion chamber T_c was measured at discrete axial position separated by 10 mm and the resulting profile was imposed as boundary condition for the LES. The temperature of the fuel injector lip T_l and the backplane T_b, instead, was measured following a procedure successfully used in previous studies [40, 41]: when the burner has reached its steady thermal state, the fuel flow is shut while the air flow is maintained. A K-type thermocouple is then applied on the surface and after a short transient due to the thermal inertia of the thermocouple, the temperature exhibits an exponential decay. This phase is extrapolated backwards to the instant of fuel shut-down, allowing to estimate the temperature during combustion. The inlet temperature of all fresh reactants is 298 K. An analytically-reduced chemical scheme for CH_4-H_2-air combustion based on 20 species and 166 reactions is used, while complex transport is modeled introducing a variable Prandtl number, Pr, and a variable nitrogen Schmidt number, Sc_{N_2}, that depend on the local molar fraction of H_2, CH_4 and N_2, as described in [38]. The inlet and outlet boundary conditions are modeled using the NSCBC formalism, which also allows to inject the targeted acoustic harmonic perturbation corresponding to the

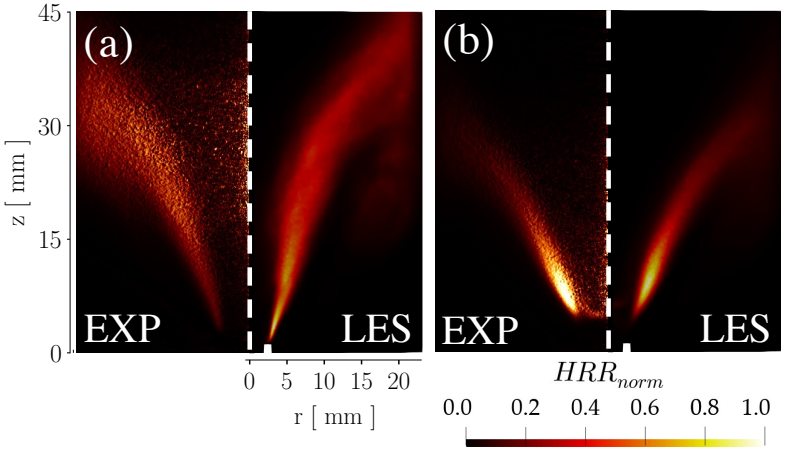

Fig. 2: Comparison between experimental Abel deconvoluted mean CH* intensity against the angle-averaged and normalized heat release rate HRR_{norm} for REF (a) and $PH10$ (b) unforced flames.

experimental acoustic forcing. Simulations were performed for roughly three forcing cycles to eliminate the initial transient. Then, at least 10 forcing cycles are simulated to gather statistics.

3. Unforced flame stabilizations and structures

This section presents the analysis of REF and $PH10$ flames in a steady flow to scrutinize the impact of the central H_2 injection on the flame characterisitcs without considering the complexity of the acoustic forcing. Figure 2 compare the experimental Abel-deconvoluted normalized CH* chemiluminescence line-of-sight integrated signal against the angle averaged normalized heat release rate (HRR_{norm}) given by LES. Figure 2(a) considers the REF case and Fig. 2(b) the $PH10$ case.

LES retrieve correctly the differences between the two injection strategies

both in terms of flame angle and flame length reduction. In presence of hydrogen pilot injection, the flame is approximately 10 mm shorter than the pure methane case. Furthermore, Fig. 2 illustrates a global redistribution of the heat release rate when pilot-H_2 is added: in the REF case, HRR_{norm} is homogeneously distributed along the entire flame brush. In the $PH10$ flame, instead, the maximum is observed at the flame root. Moreover, LES reproduces correctly the lifting of the $PH10$ flame, showing a different flame stabilization with respect to the REF one. The flame lift-off height is roughly 3 mm and is due to the presence of the central laminar hydrogen jet, as shown in Fig. 3. The comparison of the axial velocity field between the REF and $PH10$ cases in Fig. 3(a) shows that the pilot injection perturbs the Inner Recirculation Zone (IRZ) in the vicinity of the injector outlet, but it does

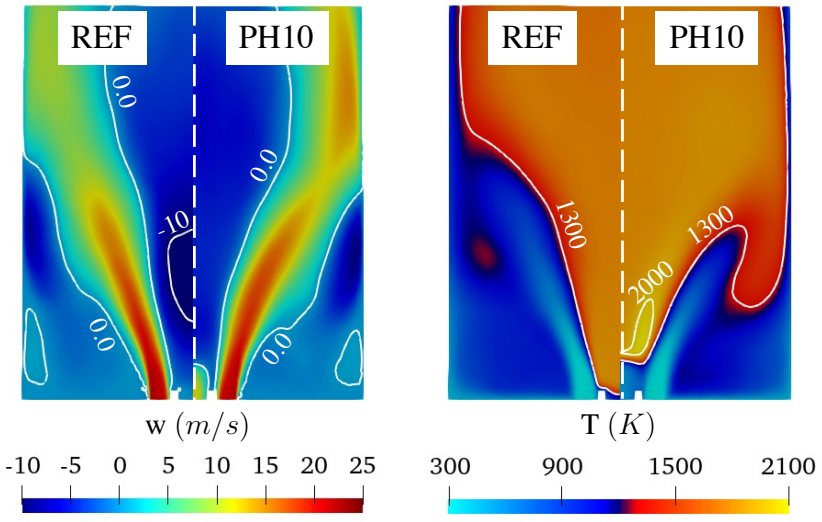

Fig. 3: Comparison of time-averaged numerical results for REF and $PH10$ in terms of axial velocity (a) and mean temperature (b) for unforced conditions.

not affect significantly the methane-air swirling jet flow. The REF flame is anchored because the burnt recirculating gas reaches the injector lip and can ignite the reactants exiting the annular channel of the injector. In the $PH10$ case, instead, the mean axial velocity field near the injector outlet is modified and the hydrogen diffusion flame prevents the hot recirculating gases from reaching the injector lip. Hence, the flame cannot ignite near the lips and the flame base stabilizes a few millimeters above the chamber backplane. Figure 3(b) shows the mean temperature field over an axial plane. The isoline at 1300 K defines the separation between fresh and hot gases for both injection strategies. The main difference occurs downstream the H_2 jet, where the pocket of high temperature above 2000 K is the result of the central hydrogen injection. To investigate this apect, the structure of the $PH10$ flame base is illustrated in Figs. 4(a-b). These figures display an axial section of an instantaneous solution, highlighting in the background the jet of the premixed CH_4-air and the pure-H_2 streams. To isolate the effect of H_2 addition, either the normalized fuel source terms and the flame indeces for both methane FI_{CH_4} and hydrogen FI_{H_2} are conditioned by the heat release rate and superimposed to the velocity fields. The flame index of the fuel F is based on the Takeno index [42], which reads:

$$FI_{\mathrm{F}} = \frac{\nabla_{\mathrm{O_2}} \cdot \nabla_{\mathrm{F}}}{\|\nabla_{\mathrm{O_2}} \cdot \nabla_{\mathrm{F}}\|} \tag{1}$$

and indicates positive or negative values as result of premixed and diffusion

combustion, respectively. Figure 4(a) shows the normalized source term of CH_4 (left) and the associated flame index (right), both conditioned by the heat release rate to ease the visualization. As expected, the positive value of the flame index confirms that methane consumption occurs in premixed mode along the main flame wing. Figure 4(b), instead, evidences that H_2 consumption takes place both along the flame wing and immediately downstream the hydrogen injection. The first is due to intermediate reactions of CH_4 oxidation, the latter is due to the combustion of H_2 pilot injection. The flame index of H_2 demonstrates that the pilot injection of hydrogen creates a diffusion branch located at the flame base, which contributes to the redistribution of heat release rate observed in Fig. 2(b) and justifies the temperature peak seen in Fig. 3(b). LES reveals also that the H_2 diffusion front is characterized by a heat release rate that is one order of magnitude lower than the maximum observed at the base of the premixed flame branch, confirming the results given by the line of sight integrated OH^* signal presented in [37].

4. Acoustically forced flames: flow dynamics and global flame response

The global FTF and the flame dynamics for REF and $PH10$ strategies are now discussed. The solid and the dotted curves in Fig. 5 show the experimental FTF in terms of gain G and phase lag φ collected over a span of forcing frequencies between 10 Hz and 600 Hz. The modulation level of the flow rate in the annular channel is set to 30% of the mean bulk velocity

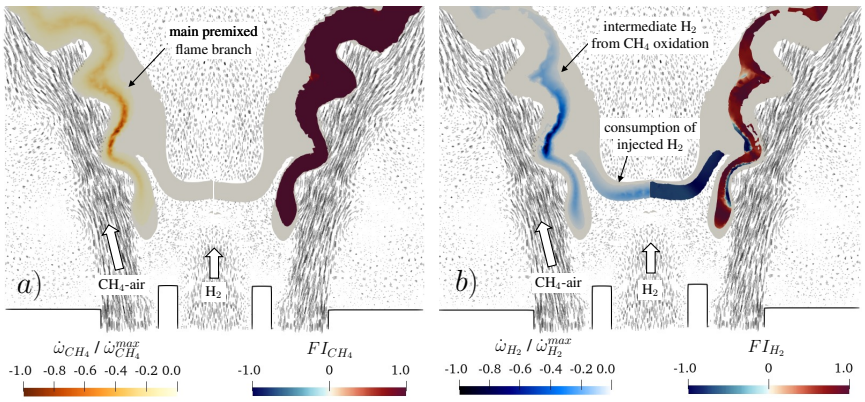

Fig. 4: Instantaneous axial cut of the $PH10$ case showing on the left the source term of CH_4 (a) and H_2 (b) conditioned by the heat release rate and on the right the associated Takeno index. The background of the images evidences the premixed CH_4-air mixture and the H_2 stream exiting the coaxial injector.

$U_b \simeq$18 m/s measured in the annular cross section of the injector. Data are sampled at 16384 Hz over a time span of 4 s. Numerical results obtained for both injection strategies at four characteristic frequencies of 100 Hz, 240 Hz, 400 Hz and 590 Hz are superposed on the experimental data, showing that the simulations accurately reproduce the trend of the FTF over the entire range of frequencies.

In the following, the dynamics at 240 Hz and 590 Hz are scrutinized. The first frequency is chosen because it corresponds to the local minimum of the FTF gain for the pilot-H_2 case while, for the second one, the difference of the FTF phase between REF and $PH10$ strategies is maximum. In this respect, Fig. 6 shows the comparison between the experimental and numerical cycle-averaged signals of acoustic pressure p' at location $L1$, the normalized acoustic velocity oscillation u'/U_b at the location $L2$ and the resulting normalized heat release rate fluctuations $\dot{Q}'/\bar{\dot{Q}}$ for REF and $PH10$ at 240 Hz

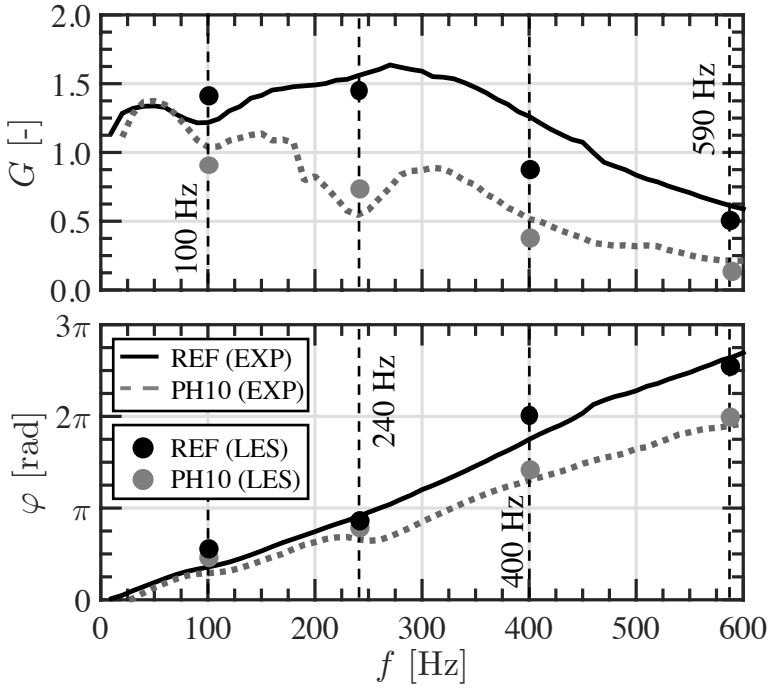

Fig. 5: Comparison between experimental and numerical FTF for the perfectly premixed methane-air mixture REF and with H_2 pilot injection $PH10$. Data are gathered for a constant thermal power $P_{\mathrm{th}} = 4$ kW and a forcing level $|u'/\mathrm{U_b}| = 0.3$.

and 590 Hz. LES data are collected with an acquisition frequency of 1 MHz to obtain smooth numerical signals and reduce the stochastic fluctuations of the flow, the time-resolved data are first spatially averaged over 20 locations homogeneously distributed at the cross section of the injector outlet and, second, cycle-averaged over more the 10 forcing cycles. In Figs. 6(a-d) numerical and experimental signals of the acoustic pressure p' are synchronized to define the beginning of the forcing cycle. The computed acoustic velocity and heat release rate oscillations are in good agreement with experiments both in terms of amplitude and relative phases. In particular, for a fixed oscillation amplitude of the axial velocity at the flame base, the fluctuation

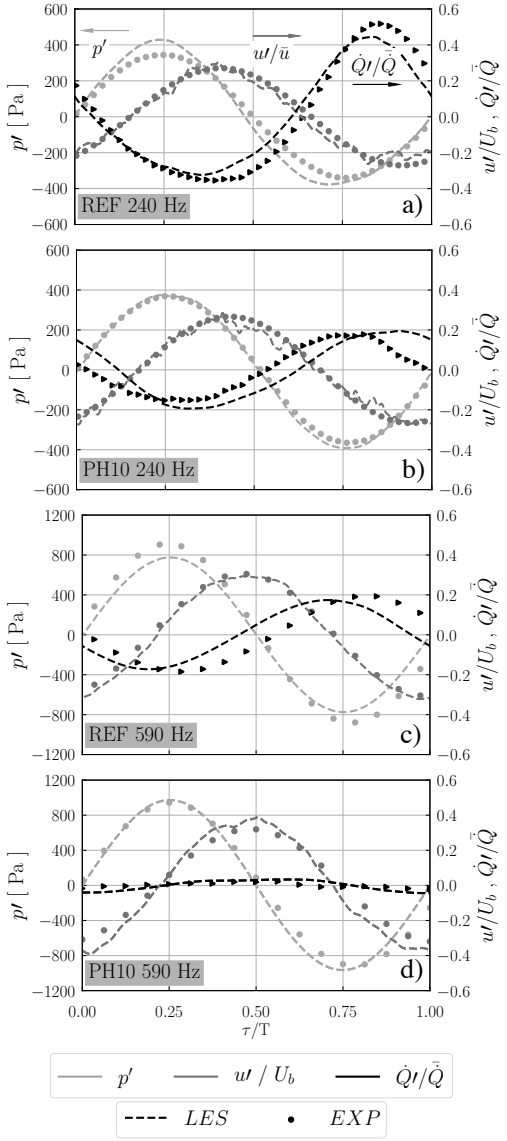

Fig. 6: Comparison between experimental and numerical cycle-averaged signals of acoustic pressure $p\prime$ ($L1$), acoustic velocity $u\prime$ ($L2$) and heat release rate fluctuation $\dot{Q}'$ for REF at 240 Hz (a), REF at 590 Hz (b), $PH10$ at 240 Hz (c) and $PH10$ at 590 Hz (d).

of the normalized heat release rate is the highest for the REF case at 240 Hz and almost zero for the $PH10$ flame at 590 Hz. These signals result respectively in the maximum and the minimum of the FTF gain obtained with

LES in Fig. 5. Furthermore, Fig. 6(a) and Fig. 6(c) show that the oscillation of the heat release rate signal obtained with LES is slightly shifted in advance with respect to the one measured in experiments, explaining the little underestimation of the FTF phase lag in Fig. 5 for the REF case. A similar behavior is displayed for the REF strategy at 590 Hz in Fig. 6(c). The results for the $PH10$ strategy at 590 Hz in Fig. 6(b), instead, show an opposite trend. The phase lag between the velocity oscillation and the heat release rate signal given by the LES is slightly larger than in experiments. This translates in a small overestimation of the FTF phase for the LES of the $PH10$ case at 240 Hz shown in Fig. 5. Finally, the $PH10$ FTF phase is correctly predicted by the LES in Fig. 6(d) and, overall, there is an excellent agreement between simulations and experiments.

4.1. Flame dynamics over the forcing cycle

The dynamics of the flame front for REF and $PH10$ are compared in Fig. 7(a-b) when forced at 240 Hz and in Fig. 8(a-b) when forced at 590 Hz. Experimental images are obtained via an inverse Abel transform of the normalized cycle-averaged line-of-sight CH* signal that is collected by a camera equipped with a narrow band interferometric filter centered o $\lambda =$ 430 nm. The associated LES images show the phase and angle-average of two fields: the normalized heat release rate HRR_{norm} and the Q-criterion Q_{crit}. The first is meant to be compared to CH* chemiluminescence images, while the second highlights intensity and position of large vortical structures during

the cycle. Both are used to interpret the interaction between the vortices and the flame front. The label on top of each image in Figs. 7 and 8 corresponds to the phase lag with respect to the harmonic pressure oscillation p' shown in Fig. 6. Simulations capture accurately the flame motion over the forcing

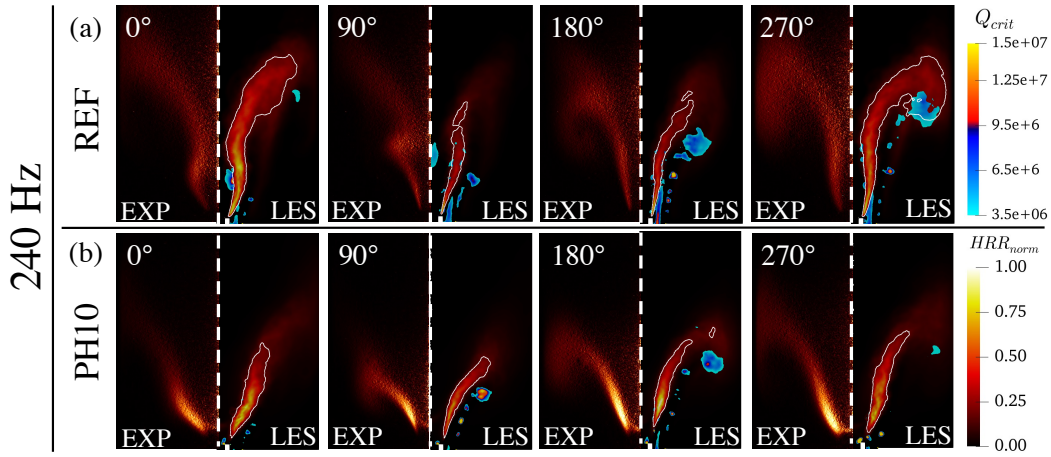

Fig. 7: Forcing frequency 240 Hz: Comparison between experimental and numerical phase averaged conditioned images of HRR for REF (a) and $PH10$ (b). Experiments (left) consider the Abel deconvoluted CH^* signal. LES results (right) present the angle-averaged fields of HRR and Q_{crit}.

cycle for all the conditions investigated. Fig. 7(a) shows that, between $\varphi = 0°$ and $90°$, the REF flame root changes its concavity and, simultaneously, the global flame length is reduced. Later in the forcing cycle the flame lengthens along the axial direction of the burner and, at $\varphi = 270°$, it shows a pronounced roll-up of the flame tip. The LES in Fig. 7(b) unveils the absence of tip roll-up for the $PH10$ flame subjected to a forcing frequency $f = 240$ Hz. Figure 8 shows the results for the forcing frequency $f = 590$ Hz and is now considered. Simulations capture a marked wrinkling of the flame front which,

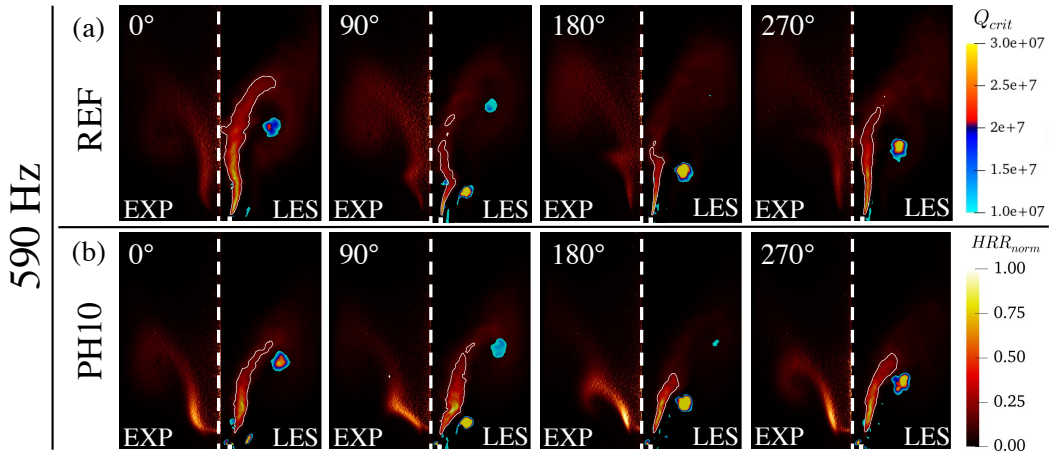

Fig. 8: Forcing frequency 590 Hz: Comparison between experimental and numerical phase averaged conditioned images of HRR for REF (a) and $PH10$ (b). Experiments (left) consider the Abel deconvoluted CH^* signal. LES results (right) present the angle-averaged fields of HRR and Q_{crit}.

as in experiments, is stronger than the one observed at 240 Hz. This is in agreement with the greater intensity of the vortical structures predicted by LES at $f = 590$ Hz. At this frequency the characteristic Strouhal number of the flow through the injector $St = fD_H/U_b$ is 0.32, where $D_H = 10$ mm is the injector hydraulic diameter and $U_b = 18$ m/s is the bulk velocity in the annular channel of the injector. This value is close to the natural shedding frequency $St \simeq 0.2$-0.3 of unswirled jets, which only weakly depends on Reynolds number [43]. The Strouhal number decreases instead to $St = 0.13$ when the flames are forced at $f = 240$ Hz and this is consistent with the lower intensity of vortices seen in the LES. Finally Figs. 7 and 8 show that, as observed for the unforced case, the hydrogen pilot injection results in the substantial increase in the burning rate at the flame base and the reduction of the flame length.

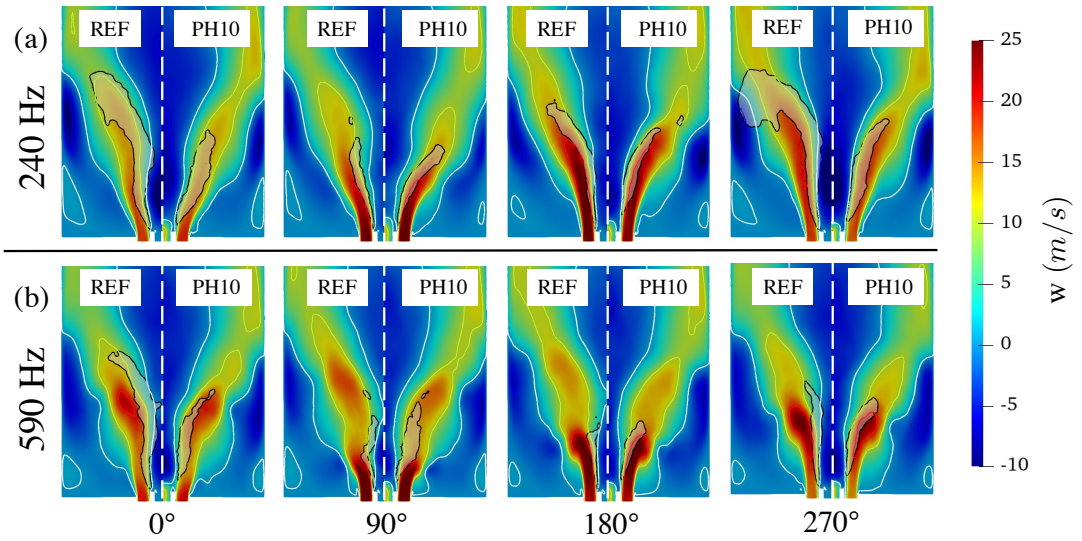

Fig. 9: REF vs $PH10$: numerical phase averaged conditioned images of axial velocity for a forcing frequency of 240 Hz (a) and 590 Hz (b). The white line defines axial velocity w = 0 m/s.

The evolution of the axial velocity fields over the acoustic cycle for the different injection strategies at 240 Hz and 590 Hz are now investigated. Figures 9(a-b) show the phase-averaged axial velocity field with the white isolines defining zero axial velocity w = 0 m/s and a black contour of the HRR_{norm} indicating the flame. LES demonstrate that the structure of the axial velocity field depends mainly on the forcing frequency with only a marginal influence of the pilot injection.

The axial velocity field in Fig. 9 at 240 Hz is now described. The two injection strategies show similar penetration of the outer swirling jet, which protrudes inside the combustion chamber with comparable angles for all the respective phases considered. Remarkably, at 240 Hz, both REF and $PH10$

exhibit a pronounced oscillation of the IRZ along the axial direction as result of the periodic velocity modulation. Between $\varphi = 0°$ and 90° the axial velocity in the annular duct increases and the IRZ is pushed downstream, whereas it moves towards the injector when the axial velocity decreases. Interestingly, this behavior is not observed when the system is forced at $f = 590$ Hz. Moreover, Fig. 9(a) shows that also the width of the IRZ changes along the forcing cycle, with an intense negative axial velocity at phases $\varphi = 270°$ and $0°$ for both REF and $PH10$. Despite the similar velocity fields observed at $f = 240$ Hz for the two injection strategies though, the interaction between the flame and the flow differs between REF and $PH10$. In the first case, the flame length variation between phase $\varphi = 90°$ and 270° is more pronounced and, while the root of the REF flame remains anchored to the injector lip, the flame base of the $PH10$ flame moves under the periodic velocity oscillation caused by the acoustic forcing. This dynamics is detailed in Fig. 10(a), which describes the position of the flame root for both injection strategies for the forcing frequency $f = 240$ Hz. The negative contour of the axial velocity $w <$ -6 m/s marks the inner recirculation zone and the isolines of the H_2 molar fraction, displayed for the $PH10$ case, indicate the penetration of the central H_2 stream. The flame root of the fully premixed case REF stabilizes in the low velocity region above the injector lip and does not move. On the contrary, the stabilization of the lifted flame for the $PH10$ case is much more sensitive to the variation of the local velocity field. The isolines of H_2 molar fraction, X_{H_2}, show a variation of the local hydrogen concentration due to

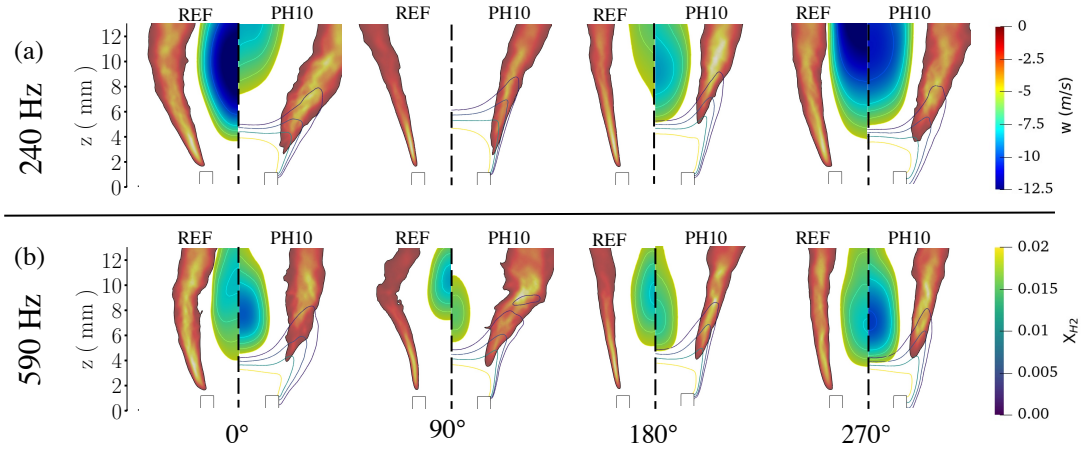

Fig. 10: Detailed view of the numerical phase averaged flame root position for REF and $PH10$ at forcing frequencies of 240 Hz (a) and 590 Hz (b). The flames are identified by the threshold $\mathrm{HRR}_{norm} > 0.1$, the IRZ and the isocontour of the H_2 molar fraction superposed.

the interaction between the central jet and the local velocity field. When the intensity of the IRZ near the injector outlet decreases ($\varphi = 90°$), the isocontour of X_{H_2} moves downstream indicating a deeper penetration of the hydrogen jet in the combustion chamber. When the IRZ moves towards the bottom, instead, the isolines of X_{H_2} are pushed towards the injector (see $\varphi = 180°$ and $\varphi = 270°$).

The axial velocity field at $f = 590$ Hz is now evaluated. Figure 9(b) presents the phase-averaged axial velocity fields that shows high velocity regions at different axial coordinates that coexist at the same phase (e.g., see phase $\varphi = 90°$), which point out a substantial change with respect to the case at 240 Hz. This can be explained by comparing the period of the forcing cycle at 590 Hz ($T_{590} = 1.7$ ms) with the characteristic convective time needed by the velocity disturbances to travel through the flame. The latter can be for

example estimated from the unforced REF flame length $h \approx 40$ mm (Fig. 2) and the time-averaged bulk flow velocity in the annular injector 18 m/s, which results in a characteristic convective time for the vortices to travel across the flame of 2.2 ms. Being the latter greater than the forcing period, a second perturbation hits the flame base before the first velocity disturbance reaches the flame tip. A further difference with respect to the flow dynamics at 240 Hz is the peak of axial velocity observed during the entire cycle at the tip of the annular jet. This is likely due to the hydrodynamic structures generated at the injector rim, which match with the vortices highlighted by the Q_{crit} contour in Fig. 8. Moreover, in contrast with the 240 Hz case, the inner recirculation zones do not undergo any relevant axial oscillations for any of the two injection strategies at 590 Hz. As consequence, Figure 10(b) shows that the isocontour of X_{H_2} in $PH10$ does not indicated any significant movement and it remains undisturbed during the whole forcing cycle. The flame root position remains fixed for both REF and $PH10$ cases. To quantify this phenomenon, Fig. 11 shows the axial position z_{root} of the flame anchoring point with respect to the injector lip over the acoustic cycle for REF and $PH10$ at 240 Hz and 590 Hz. The flame root is numerically defined as the lowest point occupied by the white contour $HRR_{norm} = 0.1$ in Figs. 7 and 8. This is superimposed to experimental measurements where the flame root is defined as the minimum axial coordinate at which 10% intensity of the Abel-deconvoluted CH^* emission signal is detected in the image. There is a good qualitative agreement between LES and experiments. In the REF

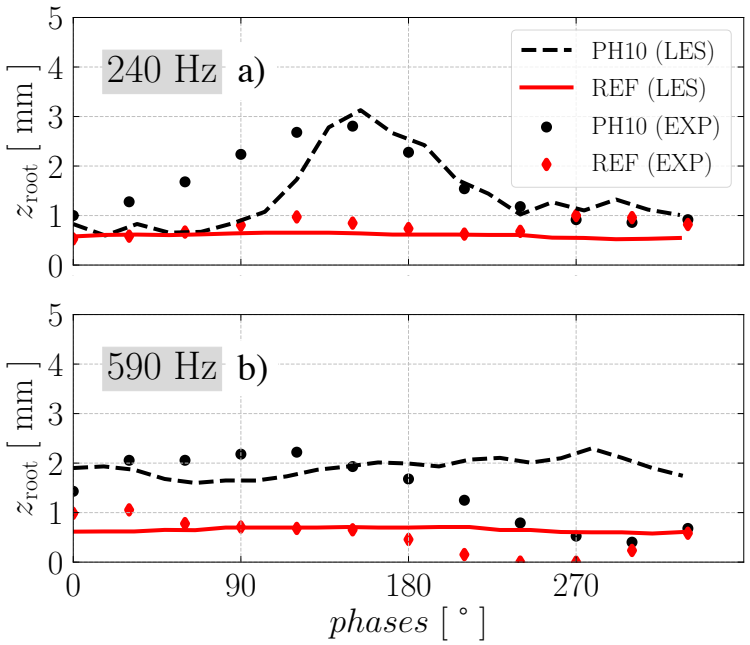

Fig. 11: Experimental and numerical flame root axial displacement with respect to the injector lip over the forcing cycle for REF and $PH10$ at 240 Hz (a) and 590 Hz (b).

case the flame root remains attached to the lip for both forcing frequencies. With hydrogen injection, instead, both experiments and LES reveal a flame root cyclic axial displacement of about 2.5 mm at 240 Hz, which corresponds roughly to 10% of the total flame length. At the higher forcing frequency of 590 Hz, the fluctuations are less pronounced. Since these oscillations interfere with the disturbances of the flame front produced by the incoming vortices, they can affect to different extents the REF and $PH10$ flame acoustic responses at different forcing frequencies. In this respect, Fig. 12 shows the maximum normalized heat release rate for a given axial coordinate (HRR^{z}_{max}) as a function of the distance z to the burner outlet for both REF (a) and $PH10$ (b) at 240 Hz. Values in Fig. 12 are conditioned by $HRR_{norm} > 0.1$

and are used to unveil either the dynamics of the flame tip or the one of the flame base during the cycle. In Fig. 12(a) is observed that the base of the REF flame remains anchored to the injector lip throug all the phases of the forcing cycle, while the flame length undergoes a periodic extension ($\varphi = 270°$ and $\varphi = 0°$) and contraction ($\varphi = 90°$ and $\varphi = 180°$) modifying the flame surface area under the influence of the velocity modulation. Figure 12(b) shows that the base of the $PH10$ flame, instead, translates along the axial direction and the heat release rate distribution is globally shifted with respect to the phase $\varphi = 0°$. In this latter case, the base of the lifted flame follows the movement of the flame tip reducing the increase of flame surface. This results corroborate the observation made in [44] where the response of an attached and a lifted swirled flame were compared finding that, in the second case, there is an additional freedom degree allowing the flame to be globally translated back and forth during the acoustic forcing cycle.

To sum up, as observed for the 240 Hz case, the phase-averaged shape of the flame over the cycle confirms that the dynamics of the REF flame differs from the $PH10$ both in terms of flame length variation and flame root movements. The impact of these aspects on the FTF gain and phase is now discussed.

4.2. FTF gain analysis

For a given harmonic velocity modulation, the gain of the FTF depends on the magnitude of the global heat release rate fluctuation $\dot{Q}'$ during the

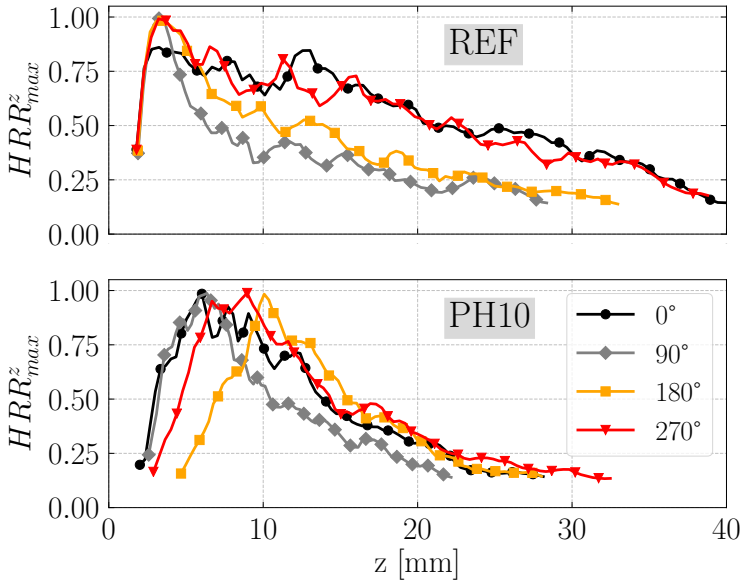

Fig. 12: Numerical distribution of the maximum heat release for a given axial coordinate HRR_z as a function to the distance z to the burner nozzle for four phases: 0°, 90°, 180°, 270° at $f = 240$ Hz. (a) REF and (b) $PH10$.

forcing cycle. This depends on the evolution of the flame surface area and the burning rate distribution along the flame brush itself [45]. Hence, the main mechanism altering flame surface wrinkling concerns the flame interaction with the large vortical structures shed at the injector rim. Changes in the burning rate along the flame determines the extent of the heat release rate variation associated to the local change of flame surface area.

The flame surface area variation resulting from interaction with hydrodynamic eddies is first considered. In this respect, it was shown in Fig. 9 that REF and $PH10$ flames are subjected to the same velocity field with vortical structure of comparable intensity when forced at the same modulation

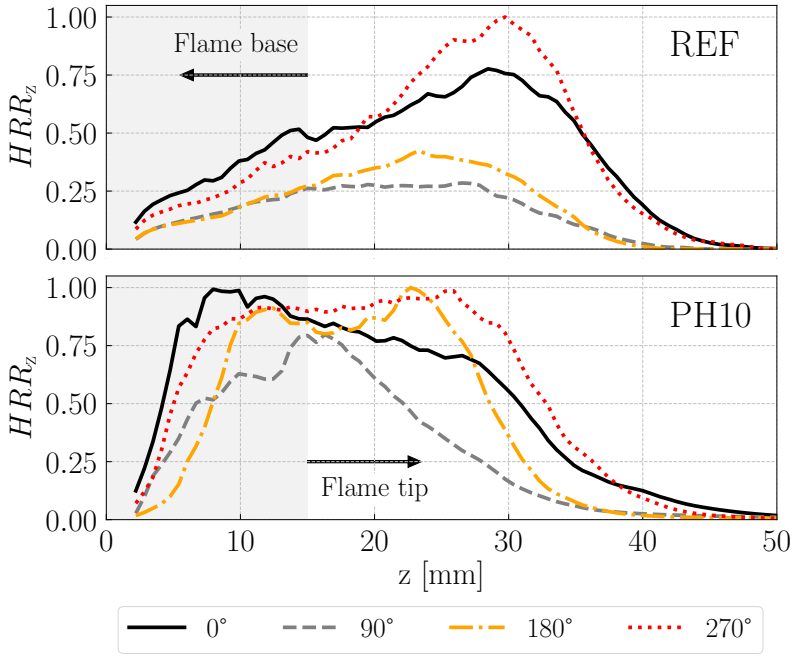

Fig. 13: Numerical distribution of the radially-integrated heat release rate with respect to the axial coordinate HRR_z for four phases: 0°, 90°, 180°, 270° at $f = 240$ Hz. (a) REF and (b) $PH10$.

frequency. Hence, the change of flame shape due to hydrogen injection does not affect the vortex shedding associated with Kelvin-Helmholtz instabilities. This is confirmed by isocontours of the Q_{crit} field in Fig. 7(a-b). At 240 Hz, eddies are released at the injector lip at phase $\varphi = 0°$ and dissipated along the flame brush before being completely consumed at the end of the forcing cycle (phase $\varphi = 270°$) for both REF and $PH10$. Remarkably, despite these similarities, the flame interaction with the vortical structures differs for the two cases. To highlight this aspect the white iso-contour corresponding to 10% of the maximum normalized heat release rate $HRR_{norm} = 0.1$ in Fig. 7 can be considered as a qualitative marker of the flame surface area evolution

through the oscillation cycle. It shows that the relative flame surface variation differs substantially between the two cases. In Fig. 7(a), the REF flame surface area changes from a minimum around phase $\varphi = 90°$ to a maximum at roughly 270° when forced at 240 Hz. This increase is driven by a vortical structure that generates a large roll up of the flame tip in Fig. 7. However, the $PH10$ flame does not undergo the same perturbation. The flame tip roll up is strongly reduced due to the reduction of the flame length caused by the H_2 addition. Figure 8 shows results at 590 Hz with similar outcomes: the REF flame undergoes a larger surface area variation with respect to the $PH10$ flame. Furthermore, despite the intensity of the eddies at 590 Hz is greater than the ones shed at 240 Hz, the tip roll up is less pronounced for the higher frequency, which is in agreement with the low FTF gain observed in this case.

The effect of H_2 pilot injection on the distribution of the heat release rate is now investigated. Figure 13 shows the axial evolution of the radially-integrated heat release rate for a given axial coordinate, HRR_z, for both REF (a) and $PH10$ (b) cases at 240 Hz. This allows to put in evidence the contribution of the different flame zones to the global heat release rate for each phase of the forcing cycle. For the REF case in Fig. 13(a), the flame response is dominated by the flame tip dynamics ($z \approx 25$ mm), at which the extent of the HRR_z reaches consistently its maximum. At $\varphi = 90°$ the flame tip is not perturbed by any vortical structure (see Fig. 7(a)) and its contribution to the global heat release rate is low. On the contrary, the flame

tip roll-up reaches its maximum at $\varphi = 270°$ and the HRR_z in this region increases. The contribution of the flame root remains negligible along the entire forcing cycle.

The response differs for $PH10$. Figure 13(b) shows that for the case $PH10$, the flame base ($z \approx 5$ mm) and the flame tip ($z \approx 25$ mm) contribute to similar extent to the overall heat release oscillation and they both influence the global flame response. This is a consequence of the redistribution of the heat release rate due to H_2 pilot injection. At $\varphi = 0°$ and $90°$, the vortical structures are absent and the largest budget of the heat release is localized near the flame root. Between $\varphi = 180°$ and $\varphi = 270°$ the vortices interfere with the flame tip (see Fig. 7(b)) and the profile of HRR_z exhibits a plateau between $z = 5$ mm and $z = 25$ mm. At these phases the contribution of the flame tip increases due to the interaction with the vortices, such as it reaches the same extent of the one at the flame base.

The global flame responses can be also analyzed by means of a Dynamic Mode Decomposition (DMD) [46] to reconstruct the spatial structure of the fluctuating component of the heat release rate at the corresponding forcing frequency and to highlight flame regions that contribute with a certain phase to the global heat release fluctuation $\dot{Q}'$ during the cycle. The DMD algorithm considers more than 200 3D-solutions for each condition. Since the flame is compact with respect to the acoustic wavelength, the acoustic pressure is considered constant over the entire computational domain and used as reference to compare simultaneously different flame regions. Figures 14(a)

and (c) show DMD results at 240 Hz and 590 Hz for both injection strategies, while Figs. 14(b) and (d) show $\dot{Q}'_{\mathrm{r}}$, the normalized radial integration of $\dot{Q}'$ along the axial coordinate, to elucidate the contribution of several parts of the flame along the burner axis. Figure 14(a) illustrates the importance of the flame roll up between $z = 20$ mm and $z = 30$ mm, near the chamber walls for the REF case (left). This is corroborated in Fig. 14(b), which shows the dominant contribution of the flame tip with respect to other flame regions. Since the REF flame is V-shaped, its acoustic response is driven by the flame tip dynamics. In fact, this accounts for most of the flame surface area variation with respect to the flame base contribution, that is closer to the burner axis. Figure 14(a) shows that for the $PH10$ case (right) the relative intensity of the heat release rate oscillation at the flame tip is reduced with respect to the REF case. To this respect, Fig. 14(b) highlights that the global heat release rate oscillation of $PH10$ is the result of an out-of-phase contribution among different parts of the flame. The redistribution of the burning rate for $PH10$ seen in Fig. 13. This generates an interference among several flame regions that partially compensate each other, leading to a gain drop. Moreover, Fig. 14(b) underlines that $PH10$ at 240 Hz, is the only operating condition showing an impact of the flame root ($z < 8$ mm) to $\dot{Q}'_{\mathrm{r}}$. This is associated to the flame root axial motion observed in Figs. 10 and 11, which makes the lower part of the flame to contribute with a certain phase to the global FTF gain, while, in the other conditions this effect is inhibited. According to the low-pass filter behavior of V-shaped swirl stabilized flames,

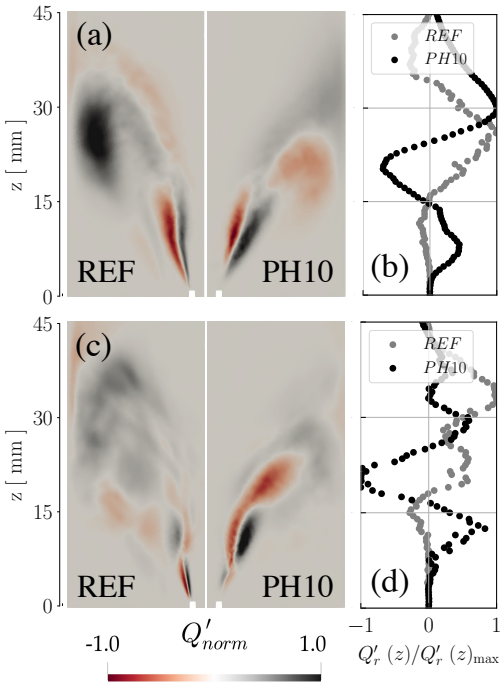

Fig. 14: Spatial distribution of heat release rate at 240 Hz (a) and 590 Hz (c) for REF (left) and $PH10$ (right) injection strategies. The axial evolution of the radial integration of these signals (right image) highlights the relative contribution of the several flame regions to the global FTF gain for 240 Hz (b) and 590 Hz (d).

DMD results at 590Hz in Fig. 14 show that, both the REF and $PH10$ flame exhibit a non-coherent response. This is mostly related to the simultaneous interference of several eddies with the flame brush during a forcing cycle, which drives down the global FTF gain (Fig. 14(d)).

4.3. FTF phase analysis

The experimental FTF phase lag φ in Fig. 5 shows that, without considering the local plateau observed for $PH10$ at 240 Hz, the slope of the two curves remains roughly constant. Hence the characteristic time delay of the two flame responses does not depend on the forcing frequency. Moreover, it

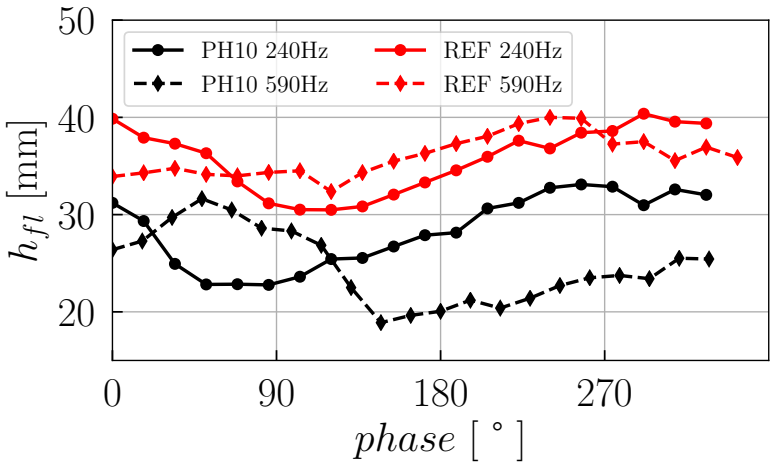

Fig. 15: Instantaneous flame height h_{fl} over the forcing cycle for REF and $PH10$ at 240 Hz and 590 Hz.

was shown in the previous section that the REF flame acoustic response is dominated by the flame tip dynamics, while $PH10$ flame exhibits an out-of-phase contribution of several flame regions. Therefore, in both cases, the entire flame length must be considered to interpret the global flame response and the delay between the velocity perturbation at the flame root and the global heat release rate oscillation. One may interpret the variation of the FTF phase shift in light of the different flame lengths. To this purpose, the mean axial convective velocity of the vortical disturbances is retrieved

Table 2: Numerical flame time lag difference $\Delta\tau$ and FTF phase shift $\Delta\varphi$ between REF and $PH10$ calculated considering the mean bulk velocity U_b and the flame height differences Δh at both 240 Hz and 590 Hz.

f	h_{REF}	h_{PH10}	Δh	$\Delta\tau{=}\Delta h/U_b$	$\Delta\varphi{=}\omega\Delta h$
Hz	mm	mm	mm	ms	rad
240	36	28	8	0.44	0.21π
590	36	25	11	0.61	0.72π

as the ratio between the mean flame length h and the time needed by these structures to reach the flame tip. This convective velocity is evaluated by tracking the axial position of the vortices released at the injector rim and results approximately $U_b = 18$ m/s, irrespective of the injection strategy adopted. Figure 15 shows the instantaneous flame height over the acoustic cycle for REF and $PH10$ at 240 Hz and 590 Hz, which is obtained numerically by considering the highest point occupied by the isocontour $HRR_{norm} = 0.1$. The mean flame height differences between REF and $PH10$ at 240 Hz and 590 Hz are Δh_{240}=8 mm and Δh_{590}=11 mm, respectively. The associated differential time lag between the two injection strategies is calculated as $\Delta\tau=\Delta h/U_b$, which leads to $\Delta\tau_{240}$=0.44 ms at 240 Hz and $\Delta\tau_{590}$=0.61 ms at 590 Hz. This translates in a phase shift $\Delta\varphi=\omega\Delta\tau$ between REF and $PH10$ equal to $\Delta\varphi_{240}$=0.21 π and $\Delta\varphi_{590}$=0.72 π (Tab. 2). These results are in good agreement with the FTF measurements in Fig. 5: $\Delta\varphi$=0.25 π at 240 Hz and 0.73 π at 590 Hz. The FTF phase reduction due to hydrogen pilot injection can be predicted considering the flame size, but it is not excluded that second order effects due to the axial redistribution of the burning rate while H_2 pilot injection might become more significant under different operating conditions.

5. Conclusion

Numerical simulations have been used to elucidate the impact of a central H_2 injection ($PH10$) on the acoustic response of CH_4-air swirling premixed

flame (REF) observed experimentally. First, LES have been used to analyze the stabilization and the flame structure associated to the two injection strategies for the unforced configurations. In the $PH10$ case the H_2 central injection reduces the global flame length, induces flame lift-off and generates a diffusion reaction front that contributes to a spatial redistribution of the heat release towards the flame base. These features are also found when the flames are subjected to acoustic forcing. Two forcing frequencies have been investigated: 240 Hz and 590 Hz. The first corresponding to the deep of the FTF gain for the $PH10$ case, the latter being representative of the maximum phase lag between the two injection strategies. LES demonstrate that the addition of H_2 injection has a negligible impact on the phase-averaged velocity field distribution, which is instead strongly dependent on the forcing frequency investigated. At $f = 240$ Hz, phase-averaged velocity fields put in evidence a significant axial oscillation of the IRZ for both injection strategies, which is instead absent at $f = 590$ Hz. Moreover, in the $PH10$ case, the movement of the IRZ affects the hydrogen jet penetration inside the combustion chamber, contributing to the flame root oscillation that affect the FTF.

Considering these results, the heat release rate distribution in different phases of the forcing cycle for the two injection strategies has been analyzed. It is shown that at 240 Hz the acoustic response of the REF flame is entirely dominated by the flame tip dynamics, while the $PH10$ flame shows an out-of-phase contribution of several flame regions that reduce the overall FTF

gain.

First, the lifting observed for the $PH10$ case makes the flame base more sensitive to the variations of the velocity field and it is able to oscillate axially under the influence of the velocity modulation. Consequently, while the REF flame is anchored to the injector lips and elongates under the influence of the velocity modulation, the entire flame front of the $PH10$ flame translates along the burner axis reducing strongly the variation of the flame surface area and, in turn, it limits the FTF gain.

Second, a marked redistribution of the heat release rate towards the flame base caused by pilot H_2 injection led to a higher contribution of this region to the global heat release rate oscillation, which is not found in the REF case.

Third, it has been shown that the reduction of the flame length observed for the $PH10$ case weakens the impact of vortical structures produced at the burner rim on the flame tip roll-up, resulting in a smaller periodic variation of the flame front surface area at both 240 Hz and 590 Hz. The DMD analysis performed at 240 Hz and 590 Hz confirm the aforementioned results and reveals that the axial displacement of the flame root, driven by the acoustic velocity modulation, can interfere with the perturbation generated by the hydrodynamic eddies affecting the resulting FTF gain.

Ultimately, LES show that the FTF phase shift between the injection strategies can be predicted by considering the time lag variations associated to the change of the flame length. However, this does not exclude that the

impact of the redistribution of the heat release rate due to H_2 pilot injection could become a dominant mechanism at different operating conditions.

Acknowledgments

This project has received funding from the ERC H2020 Grant Agreement 832248 (SCIROCCO). HPC resources from GENCI (Allocations A0092B10627 and A0112B10627) and PRACE projects 2020225434 (FANTASTIC-H2) and 2021240098 (WONDER) are also highly acknowledged.

References

[1] H. H. W. Funke, N. Beckman, J. Keinz, A. Horikawa, 30 years of dry low NO_x micromix combustor research for hydrogen-rich fuels: an overview of past and present activities, J. Eng. Gas Turbines Power 143 (2020) 071002 (13 pages).

[2] M. R. Bothien, A. Ciani, J. P. Wood, G. Fruechtel, Toward Decarbonized Power Generation With Gas Turbines by Using Sequential Combustion for Burning Hydrogen, J. Eng. Gas Turbines Power 141, 121013 (11 2019).

[3] T. Poinsot, Prediction and control of combustion instabilities in real engines, Proc. Combust. Inst. 36 (2017) 1–28.

[4] T. Lieuwen, V. Yang (Eds.), Combustion instabilities in gas turbine engines: operational experience, fundamental mechanisms and modeling,

Progress in astronautics and aeronautics, American Institute of Aeronautics and Astronautics, 2005.

[5] J. O'Connor, Understanding the role of flow dynamics in thermoacoustic combustion instability, Proc. Combust. Inst. (2022) In press-doi:https://doi.org/10.1016/j.proci.2022.07.115.

[6] A. L. Sánchez, F. A. Williams, Recent advances in understanding of flammability characteristics of hydrogen, Prog. Energy Combust. Sci. 41 (2014) 1–55.

[7] B. Milton, J. Keck, Laminar burning velocities in stoichiometric hydrogen and hydrogen-hydrocarbon gas mixtures, Combust. Flame 58 (1984) 13–22.

[8] F. Halter, C. Chauveau, N. Djebaïli-Chaumeix, I. Gökalp, Characterization of the effects of pressure and hydrogen concentration on laminar burning velocities of methane–hydrogen–air mixtures, Proc. Combust. Inst. 30 (2005) 201–208.

[9] G. Yu, C. Law, C. Wu, Laminar flame speeds of hydrocarbon + air mixtures with hydrogen addition, Combust. Flame 63 (1986) 339–347.

[10] G. S. Jackson, R. Sai, J. M. Plaia, C. M. Boggs, K. T. Kiger, Influence of H_2 on the response of lean premixed CH_4 flames to high strained flows, Combust. Flame 132 (2003) 503–511.

[11] O. Kwon, G. Faeth, Flame/stretch interactions of premixed hydrogen-fueled flames: measurements and predictions, Combust. Flame 124 (2001) 590–610.

[12] R. Schefer, D. Wicksall, A. Agrawal, Combustion of hydrogen-enriched methane in a lean premixed swirl-stabilized burner, Proc. Combust. Inst. 29 (2002) 843 – 851.

[13] Y. Huang, V. Yang, Bifurcation of flame structure in a lean-premixed swirl-stabilized combustor: transition from stable to unstable flame, Combust. Flame 136 (2004) 383–389.

[14] H. S. Kim, V. K. Arghode, M. B. Linck, A. K. Gupta, Hydrogen addition effects in a confined swirl-stabilized methane-air flame, Int. J. Hydrog. Energy 34 (2009) 1054–1062.

[15] T. Guiberti, D. Durox, P. Scouflaire, T. Schuller, Impact of heat loss and hydrogen enrichment on the shape of confined swirling flames, Proc. Combust. Inst. 35 (2015) 1385 – 1392.

[16] Q. An, A. M. Steinberg, The role of strain rate, local extinction, and hydrodynamic instability on transition between attached and lifted swirl flames, Combust. Flame 199 (2019) 267–278.

[17] P. L. Therkelsen, J. E. Portillo, D. Littlejohn, S. M. Martin, R. K. Cheng, Self-induced unstable behaviors of CH_4 and H_2/CH_4 flames in a

model combustor with a low-swirl injector, Combust. Flame 160 (2013) 307–321.

[18] I. Chterev, I. Boxx, Effect of hydrogen enrichment on the dynamics of a lean technically premixed elevated pressure flame, Combust. Flame 225 (2021) 149–159.

[19] J. G. Aguilar, E. Æsøy, J. R. Dawson, The influence of hydrogen on the stability of a perfectly premixed combustor, Combust. Flame 245 (2022) 112323.

[20] D. Davis, P. Therkelsen, D. Littlejohn, R. Cheng, Effects of hydrogen on the thermo-acoustics coupling mechanisms of low-swirl injector flames in a model gas turbine combustor, Proc. Combust. Inst. 34 (2013) 3135–3143.

[21] J. Beita, M. Talibi, S. Sadasivuni, R. Balachandran, Thermoacoustic instability considerations for high hydrogen combustion in lean premixed gas turbine combustors: A review, Hydrogen 2 (2021) 33–57.

[22] E. Æsøy, J. G. Aguilar, S. Wiseman, M. R. Bothien, N. A. Worth, J. R. Dawson, Scaling and prediction of transfer functions in lean premixed H_2/CH_4-flames, Combust. Flame 215 (2020) 269–282.

[23] Z. Lim, J. Li, A. S. Morgans, The effect of hydrogen enrichment on the forced response of CH_4/H_2/air laminar flames, Int. J. Hydrog. Energy 46 (2021) 23943–23953.

[24] A. Ghani, W. Polifke, Control of intrinsic thermoacoustic instabilities using hydrogen fuel, Proc. Comb. Inst. 38 (2021) 6077–6084.

[25] D. Kim, S. W. Park, Effects of hydrogen addition on flame structure and forced flame response to velocity modulation in a turbulent lean premixed combustor, Fuel 89 (2010) 3475–3481.

[26] H. Kutkan, A. Amato, G. Campa, G. Ghirardo, L. Tay Wo Chong, E. Æsøy, Modeling of Turbulent Premixed CH_4/H_2/Air Flames Including the Influence of Stretch and Heat Losses, J. Eng. Gas Turbines Power 144 (10 2021).

[27] P. Palies, T. Schuller, D. Durox, L. Gicquel, S. Candel, Acoustically perturbed turbulent premixed swirling flames, Phys. Fluids 23 (2011) 037101.

[28] S. Kwak, J. Choi, M. Ahn, Y. Yoon, Effects of hydrogen addition on the forced response of H_2/CH_4 flames in a dual-nozzle swirl-stabilized combustor, Int. J. Hydrog. Energy 47 (2022) 28139–28151.

[29] J. Strollo, S. Peluso, J. O'Connor, Effect of Hydrogen on Steady-State and Transient Combustion Instability Characteristics, J. Eng. Gas Turbines Power 143 (2021) 071023 (12 pages).

[30] T. Indlekofer, B. Ahn, Y. H. Kwah, S. Wiseman, M. Mazur, J. R. Dawson, N. A. Worth, The effect of hydrogen addition on the amplitude and

harmonic response of azimuthal instabilities in a pressurized annular combustor, Combust. Flame 228 (2021) 375–387.

[31] S. Barbosa, M. de La Cruz Garcia, S. Ducruix, B. Labegorre, F. Lacas, Control of combustion instabilities by local injection of hydrogen, Proc. Combust. Inst. 31 (2007) 3207 – 3214.

[32] K. T. Kim, S. Hochgreb, Effects of nonuniform reactant stoichiometry on thermoacoustic instability in a lean-premixed gas turbine combustor, Combust. Sci. Technol. 184 (2012) 608–628.

[33] A. Katoch, T. F. Guiberti, D. V. de Campos, D. A. Lacoste, Dual-fuel, dual-swirl burner for the mitigation of thermoacoustic instabilities in turbulent ammonia-hydrogen flames, Combust. Flame 246 (2022) 112392.

[34] J. Li, H. Kwon, D. Seksinsky, D. Doleiden, J. O'Connor, Y. Xuan, M. Akiki, J. Blust, Describing the Mechanism of Instability Suppression Using a Central Pilot Flame With Coupled Experiments and Simulations, J. Eng. Gas Turbines Power 144 (10 2021).

[35] D. Doleiden, A. Karmarkar, J. O'Connor, J. Blust, Impact of central piloting on the static and dynamic stability of swirl-stabilized flames, in: ASME Turbo Expo, Paper No. GT2022-80226, 2022.

[36] G. Oztarlik, L. Selle, T. Poinsot, T. Schuller, Suppression of instabilities

of swirled premixed flames with minimal secondary hydrogen injection, Combust. Flame 214 (2020) 266 – 276.

[37] T. Schuller, S. Marragou, G. Oztarlik, T. Poinsot, L. Selle, Influence of hydrogen content and injection scheme on the describing function of swirled flames, Combust. Flame 240 (2022) 111974.

[38] D. Laera, P. Agostinelli, L. Selle, Q. Cazères, G. Oztarlik, T. Schuller, L. Gicquel, T. Poinsot, Stabilization mechanisms of CH_4 premixed swirled flame enriched with a non-premixed hydrogen injection, Proc. Combust. Inst. 38 (2021) 6355–6363.

[39] J.-P. Legier, T. Poinsot, D. Veynante, Dynamically thickened flame les model for premixed and non-premixed turbulent combustion, in: Proceedings of the summer program, Vol. 12, 2000.

[40] Y. Ding, D. Durox, N. Darabiha, T. Schuller, Chemiluminescence of burner-stabilized premixed laminar flames, Combust. Sci. Technol. 191 (1) (2019) 1–25. doi:10.1080/00102202.2018.1558391.

[41] A. Aniello, T. Poinsot, L. Selle, T. Schuller, Hydrogen substitution of natural-gas in premixed burners and implications for blow-off and flashback limits, Int. J. Hydrog. Energy 47 (2022) 33067–33081.

[42] H. Yamashita, M. Shimada, T. Takeno, A numerical study on flame stability at the transition point of jet diffusion flames, Symposium (International) on Combustion 26 (1996) 27–34.

[43] B. Emerson, J. O'Connor, M. Juniper, T. Lieuwen, Density ratio effects on reacting bluff-body flow field characteristics, J. Fluid Mech. 706 (2012) 219–250.

[44] M. Gatti, R. Gaudron, C. Mirat, L. Zimmer, T. Schuller, Impact of swirl and bluff-body on the transfer function of premixed flames, Proceedings of the Combustion Institute 37 (4) (2019) 5197–5204.

[45] T. Schuller, T. Poinsot, S. Candel, Dynamics and control of premixed combustion systems based on flame transfer and describing functions, J. Fluid Mech 894 (2020) P1.

[46] P. J. Schmid, Dynamic mode decomposition of numerical and experimental data, J. Fluid Mech. 656 (2010) 5–28.